Technical Design Considerations of a Human-Scale Talbot-Lau Interferometer for Dark-Field CT

Manuel Viermetz, Nikolai Gustschin, Clemens Schmid, Jakob Haeusele, Peter B. Noël, *Member, IEEE*, Roland Proksa, Stefan Löscher, Thomas Koehler, and Franz Pfeiffer

***Abstract*— Computed tomography (CT) as an important clinical diagnostics method can profit from extension with dark-field imaging, as it is currently restricted to X-rays' attenuation contrast only. Dark-field imaging allows access to more tissue properties, such as micro-structural texture or porosity. The up-scaling process to clinical scale is complex because several design constraints must be considered. The two most important ones are that the finest grating is limited by current manufacturing technology to a 4.8 μm period and that the interferometer should fit into the CT gantry with minimal modifications only. In this work we discuss why an inverse interferometer and a triangular G_1 profile are advantageous and make a compact and sensitive interferometer implementation feasible. Our evaluation of the triangular grating profile reveals a deviation in the interference pattern compared to standard grating profiles, which must be considered in the subsequent data processing. An analysis of the grating orientation demonstrates that currently only a vertical layout can be combined with cylindrical bending of the gratings. We also provide an in-depth discussion, including a new simulation approach, of the impact of the extended X-ray source spot which can lead to large performance loss and present supporting experimental results. This analysis reveals a vastly increased sensitivity to geometry and grating period deviations, which must be considered early in the system design process.**

***Index Terms*— Computed tomography, dark-field contrast, Talbot-Lau interferometer, X-ray imaging.**

I. Introduction

X-RAY computed tomography (CT) is a well-established technique for non-destructive three-dimensional imaging of objects. Especially in medical imaging CT is important as it quickly provides high-resolution images for radiologic diagnostics. Its applications are widespread and flexible, which was recently proven with rapid COVID-19 diagnostics based on lung CT [1]. Ongoing technological development has brought dual-energy and photon-counting technology to clinics, allowing better use of contrast agents and a decrease of patient dose.

Another candidate to extend the value of clinical CT is dark-field imaging which allows to simultaneously measure the attenuation, refraction, and small-angle scattering of a transmitted sample [2], [3], [4]. While this can be achieved with various methods at synchrotrons (e.g., analyzer-based, speckle-based, propagation-based imaging [5], [6], [7]) only grating-based Talbot-Lau interferometry and edge illumination have successfully been translated to incoherent X-ray sources with a large source spot [8], [9], [10], [11].

Added diagnostic value from dark-field imaging has been demonstrated in numerous studies at synchrotron and laboratory implementations. It was shown that the dark-field modality in particular can enhance lung diagnostics as it enables the detection of micro-structural changes in lung parenchyma, which is not possible with any other imaging method [12], [13], [14], [15], [16], [17], [18]. Similar results have also been found for dark-field CT in laboratory experiments, albeit limited to small fields of view and long scan times of several minutes to hours [17], [18], [19]. Recent milestones have been the first clinical dark-field chest radiography system and the demonstration of the diagnostic value of dark-field signal for lung imaging of human patients [20].

Manuscript received 31 May 2022; revised 2 August 2022; accepted 14 September 2022. Date of publication 16 September 2022; date of current version 29 December 2022. This work was supported in part by the Karlsruhe Nano Micro Facility (KNMF, www.kit.edu/knmf), a Helmholtz Research Infrastructure at Karlsruhe Institute of Technology (KIT); in part by the TUM Institute for Advanced Study; in part by the European Research Council (ERC H2020), under Grant AdG 695045; and in part by Philips DACH GmbH. *(Corresponding author: Manuel Viermetz.)*

Manuel Viermetz, Nikolai Gustschin, Clemens Schmid, and Jakob Haeusele are with the Chair of Biomedical Physics, Department of Physics, Technical University of Munich, 85748 Garching, Germany, and also with the Munich Institute of Biomedical Engineering, Technical University of Munich, 85748 Garching, Germany (e-mail: manuel.viermetz@tum.de; nikolai.gustschin@tum.de; clemens.schmid@tum.de; jakob.haeusele@tum.de).

Peter B. Noël was with the Department of Diagnostic and Interventional Radiology, School of Medicine and Klinikum rechts der Isar, Technical University of Munich, 81675 Munich, Germany. He is now with the Department of Radiology, Perelman School of Medicine, University of Pennsylvania, Philadelphia, PA 19104 USA (e-mail: peter.noel@pennmedicine.upenn.edu).

Roland Proksa and Stefan Löscher are with Philips Research, 22335 Hamburg, Germany (e-mail: roland.proksa@philips.com; stefan.loescher@philips.com).

Thomas Koehler is with Philips Research, 22335 Hamburg, Germany, and also with the Institute for Advanced Study, Technical University of Munich, 85748 Garching, Germany (e-mail: thomas.koehler@philips.com).

Franz Pfeiffer is with the Department of Diagnostic and Interventional Radiology, Klinikum rechts der Isar, Technical University of Munich, 81675 Munich, Germany, also with the Institute for Advanced Study, Technical University of Munich, 85748 Garching, Germany, also with the Chair of Biomedical Physics, Department of Physics, Technical University of Munich, 85748 Garching, Germany, and also with the Munich Institute of Biomedical Engineering, Technical University of Munich, 85748 Garching, Germany (e-mail: franz.pfeiffer@tum.de).

Digital Object Identifier 10.1109/TMI.2022.3207579

To realize dark-field CT imaging for clinical application, however, non-trivial adaptations to the challenging environment of a rotating CT gantry and the only 1 m long beam path are required. In our recently published paper [21] we demonstrated the feasibility of such systems and presented first reconstruction results of dark-field images at human scale from our prototype implementation. In this paper, we now focus on the technical details and our design considerations which led to this prototype system. In contrast to other grating-based imaging devices, an extremely compact design adapted to the strong beam divergence and the hard X-ray spectrum in clinical CT is required. We analyze different interferometer geometries, the impact on the sensitivity, potential grating fabrication methods, and which grating profile is most promising. We here focus on binary absorption gratings and triangular grating profile as G_1 candidates. The latter of those profiles, however, has only once before been used in an X-ray Talbot-Lau interferometer [22], thus there is limited experience. We therefore evaluate the impact of the non-binary profile on the interferometer in detail. Other important topics are grating orientation and the large source spot of the clinical X-ray tube. A comprehensive simulation is proposed to include the large width of the focal spot. We derive how its width impacts the performance of the interferometer, revealing why grating fabrication tolerances in clinical dark-field CT are significantly tighter than at laboratory systems.

II. Requirements for Clinical Dark-Field CT

Our objective is to combine the dark-field imaging technology with a state-of-the-art clinical CT system to provide high-resolution imaging at a fast acquisition time over a human patient sized field of view. The primary application of such a device is currently imaging of the human lung, motivated by results from dark-field radiography (2D-imaging) patient studies [20].

To head start development, the system is based on a conventional clinical CT to benefit from decades of development and optimization. These systems come with highly specialized X-ray sources and detectors, which are fully compatible with dark-field imaging. Furthermore, a modified medical system is advantageous to appeal for approval (e.g., for clinical use) as most components remain unchanged. The only drawbacks are limitations in the design freedom since modifications of the provided infrastructure should be kept to a minimum.

As a base system, a CT gantry with a single X-ray source and a sufficient power overhead is favorable. This allows to keep the complexity of the system low and to compensate the absorption of flux in the added components of the grating interferometer. A multi-line detector is advantageous to have short acquisition times, which is important for chest scans where a breath-hold is required. Furthermore, a 2D detector image provides better orientation during grating adjustment. Technical aspects, such as the size of the collimator box and the accessibility of the area in front of the detector, are crucial for being able to integrate the gratings and their mounts into the system. The amount of vibrations produced by the gantry rotation and the various components on the gantry can also have a significant impact on the interferometer performance, but are difficult to assess in advance.

As has recently been demonstrated in [21], the Philips Brilliance iCT SP is a suitable candidate as a base system for a dark-field CT. Its geometry is similar to most clinical CTs on the market (source-iso-center distance around 55 cm and detector-iso-center distance around 45 cm), it has only one high-power X-ray tube (120 kW), and 64 detector lines. After removal of its ultra-high-resolution comb the area in front of the anti-scatter grid and the detector is accessible for implementation of gratings and the modular collimator box can easily be modified. The only presumably important difference compared to other vendors' models is the air bearing of the gantry [23] which decouples the gantry from the surrounding environment and is assumed to avoid vibrations, which ball bearings used in other systems might create. Nevertheless, the vibrations from on-gantry components remain, and it is currently not clear if this bearing is really required.

III. Talbot-Lau Interferometer Geometries

With a Talbot-Lau interferometer the three contrast channels attenuation, phase-shift, and dark-field are measured. The implementation at an incoherent X-ray source requires three gratings, referred to as G_0, G_1, and G_2. The G_1 introduces a fine modulation on the incident radiation causing a corresponding interference pattern in the plane of the G_2. Attenuation of the radiation by the sample causes a decrease of intensity while refraction and small-angle scattering induce shift and blurring of the resulting pattern, respectively. To retrieve the sub-pixel changes of the pattern with a conventional detector an *analyzer grating* G_2 is positioned in front of the detector, which has the same periodicity as the intensity modulation and leads to a Moiré pattern. The *source grating* G_0 is used to separate the incoherent source into periodic slit sources, which fulfill the coherence requirement for the length of the interferometer setup. A common measure to quantify the performance of such an interferometer is the visibility of the Moiré pattern measured by the detector as defined in [2] and [10].

We distinguish between three interferometer geometries as derived by Donath *et al.* in [24], namely symmetric, asymmetric, and inverse geometry. The grating periods p_0 and p_2 of the G_0 and G_2 strongly depend on the selected G_1 period p_1 and the interferometer geometry following the relations,

$$p_0 = \frac{L+d}{d}\, p_1 \quad \text{, and} \tag{1}$$

$$p_2 = \frac{L+d}{L}\, p_1 \,, \tag{2}$$

for absorption or $\pi/2$ phase-shifting G_1 with L and d denoting the distances between G_0 and G_1, and G_1 and G_2, respectively.

The simplest design is a symmetric geometry where G_1 is positioned halfway between G_0 and G_2, i.e., $L = d$. This design yields a high sensitivity and simplifies the grating fabrication process since at least G_0 and G_2 have the same period. For laboratory setups where setup length and sample position are only weakly constrained this geometry is therefore popular and has been successfully implemented in numerous setups [25], [26], [27], [28]. Conversely, for a clinical CT the

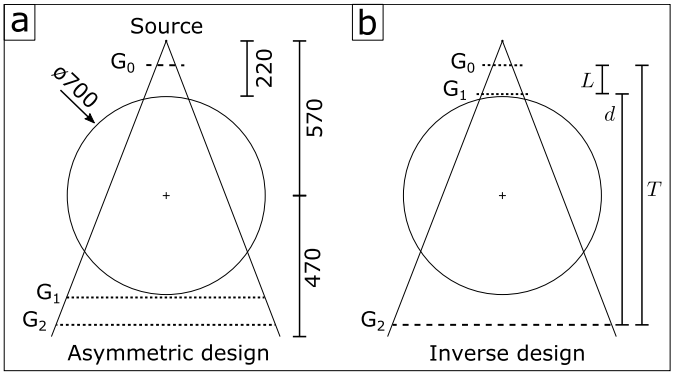

Fig. 1. Asymmetric and inverse interferometer geometries. a, The dimensions of the clinical CT gantry limit where the three gratings of the Talbot-Lau interferometer can be positioned. An asymmetric geometry fully exploits the otherwise empty space between detector and patient at the cost of a large G_1 and G_2 with fine periods. b, In the inverse geometry, G_0 and G_1 must be implemented into the collimator box and have finer periods than the large G_2. Since G_1 is in front of the patient, it decreases the patient dose and is smaller than in the asymmetric geometry, making it easier to fabricate.

symmetric geometry does not work as it would require the G_1 to be positioned within the patient area.

An alternative design is the asymmetric (or conventional) geometry, which is sketched in Fig. 1a. It is suitable for implementation in a clinical CT geometry as it provides sufficient room for positioning the patient. However, as illustrated and given by Equations (1) and (2), the grating periods of the large G_1 and G_2 are the finest in this design. Since current grating fabrication cannot produce sufficiently large gratings to cover the area in front of a CT detector (approximately 80 cm), both gratings must be combined from several smaller grating tiles. These aspects make implementation and adjustment complicated and prone to instabilities, particularly as combining fine pitch gratings requires a high precision to avoid artifacts [29]. Furthermore, fabrication of large areas with fine grating periods is often inefficient because of an increased defect rate.

With the inverse interferometer geometry, which is basically a reversed asymmetric geometry as shown in Fig. 1b, most identified problems can be solved. It results in the advantage that the gratings with fine periods only need to cover a small area compared to the asymmetric geometry. With recent advances in grating fabrication the G_1 can now be fabricated as one piece which makes G_2 the only grating to be combined from smaller tiles. Since the G_2 has the coarsest period, fabrication has a low defect-rate and can efficiently produce high-quality tiles. This makes implementation significantly less complex and more stable than in the asymmetric geometry. Furthermore, the inverse geometry is advantageous to minimize patient dose because even if G_1 is implemented as a phase-grating it absorbs a significant fraction of the incoming X-ray flux. For example, in the prototype design published in [21] the G_1 absorbs 12.5% of the incoming flux. Since this absorption is in front of the patient it does not lead to an increase of the patient dose. Additionally, the high-quality of the G_2 ensures that radiation which passed the patient is not lost in a defect and thus ensures dose efficiency. We conclude that with current grating fabrication technology the inverse geometry is favorable for clinical dark-field CT implementation and the following considerations are based on this geometry.

In our dark-field CT prototype the implementation of the inverse geometry has been achieved by integrating the G_0 and G_1 with a custom grating mount into the collimator box. The compact G_0 and G_1 assembly comes pre-adjusted from a laboratory setup and then replaces the bow-tie filter unit of the original system. This leaves critical components, such as the collimator blades, untouched and minimizes adjustment in the gantry. The component can be manually rotated along cone- and fan-angle, and it can be shifted parallel to the CT rotation axis with a motor of the former bow-tie filter. The large G_2 replaces the ultra-high-resolution comb, which is an optional feature in clinical CT to boost the spatial resolution of the CT reconstruction [30]. Since our objective focuses on lung imaging, removal of this component, which is primarily used for inner ear diagnostics, comes with no drawback. The G_2 is not retractable and is adjusted manually with custom-made G_2 positioning mechanics to keep the complexity of the implementation low.

This discussion and the results in [21] demonstrate that implementation of an inverse Talbot-Lau interferometer can be realized in an iCT or a similar gantry with minor modifications. Since G_0 and G_1 periods cannot be arbitrarily fine due to fabrication limitations and the distance between them has to be short to fit G_0 and G_1 into the confined space inside the collimator box, the system sensitivity is limited by these parameters as follows.

The angular sensitivity S, a common performance measure for Talbot-Lau interferometers, characterizes the minimal resolvable refraction angle and is given in inverse geometry by:

$$S = \left(\frac{1}{L} + \frac{1}{d}\right)^{-1} \frac{1}{p_1}\left(1 - \frac{x}{d}\right) = \frac{d}{p_2}\left(1 - \frac{x}{d}\right) \tag{3}$$

It depends on the geometry of the setup, the periods of the gratings, and the distance x of the sample to G_1 [24]. From this we can conclude that a long geometry, a more symmetric geometry (at a given total length), and small grating periods increase the sensitivity and thus enhance interferometer performance. While these aspects are purely design related, the position dependence of S leads to two inconveniences during interpretation of the measured data: (1) The sensitivity has its maximum closest to G_1 and otherwise decreases linearly towards G_2, consequently the patient (positioned in the isocenter, i.e., not near the G_1) is examined with a reduced sensitivity. (2) Since the patient extends over a significant area there is a sensitivity gradient along the ray path which must be considered during reconstruction. A solution which cleanly solves this issue during filtered backprojection reconstruction can be found in [31].

Another important design measure in dark-field setups is the correlation length ξ, which can be calculated from the sensitivity [16], [32], [33], [34]:

$$\xi = S \cdot \lambda \tag{4}$$

This now includes the wavelength λ as a dependency of the small-angle scattering sensitivity and goes beyond the spectral performance of the interferometer components themselves (i.e., performance of X-ray absorption gratings). A recent study suggests a correlation length of around 1 µm for lung imaging, which has been derived from several measurements with pig lungs at a specialized radiography setup [16]. Such a long correlation length requires a highly sensitive setup and is challenging to achieve, particularly in clinical designs. Therefore, we want to emphasize that there are several implementations with lower correlation length which still perform well in dark-field imaging of the lung [18], [20], [35]. For example, in [36] human thorax dark-field radiographies are presented at a correlation length around 0.5 µm.

Considering these aspects, clinical dark-field CT should use a soft X-ray spectrum as this maximizes the correlation length and increases performance of the absorption gratings in the interferometer. Consequently, at our prototype system a 80 kVp spectrum is used, which is the lowest available kVp setting for the Brilliance iCT platform. As this is a relatively soft X-ray spectrum for clinical CT this can limit the patient size because attenuation in lateral projections can cause artifacts due to photon starvation, hence, it is advantageous if the X-ray tube has a power overhead. With the arising limitation to a maximum patient size we decided for our prototype implementation on a 45 cm instead of the conventional 50 cm diameter field of view. This also simplifies installation of G_0 and G_1 because not the full fan opening must be covered, leaving more space for the mount and the adjustment mechanics.

IV. Grating Design and Parameterization

The periods and structure heights of the gratings are key parameters for successful dark-field imaging, but as grating fabrication is a complex and time-consuming process all aspects and limitations must be considered. Trade-offs between finer periods, higher structures, and feasibility of defect-free fabrication are unavoidable.

For a clinical dark-field CT operated with a 80 kVp spectrum particularly the two absorption gratings G_0 and G_2 are difficult to fabricate. This is because their grating structure heights must be pushed to the current fabrication limits in order to obtain good absorption even for this rather soft clinical spectrum. Gold is used for the grating bars as it has excellent absorption properties, but the lamella of both gratings must still be higher than 200 µm for sufficient stopping power.

For our proposed design we concentrate on grating structures fabricated using the LIGA process by the Karlsruhe Institute of Technology (KIT) and microworks GmbH [29], [37], [38]. Fig. 2 illustrates the fabrication process using X-ray lithography which has a remarkable scalability towards large resist thicknesses and high aspect-ratios. While in this illustration only an aspect-ratio (i.e., lamella height vs. width) of five is shown, the LIGA process currently achieves aspect-ratios exceeding 100 for grating periods of 4.8 µm with minimal defects [37].

For these high aspect-ratios, stabilization bridges between the resist lamella must be included in the layout, since otherwise the structures easily distort or collapse between development and electroplating. The drawback of this addition is some loss of grating area and thus interferometer performance. The percentage of lost area is referred to as *bridge fraction* and usually lies between 1% and 10%. Consequently, a trade-off between few bridges, which can lead to defects and in-homogeneous grating quality, and too many bridges must be found to minimize the interferometer performance loss.

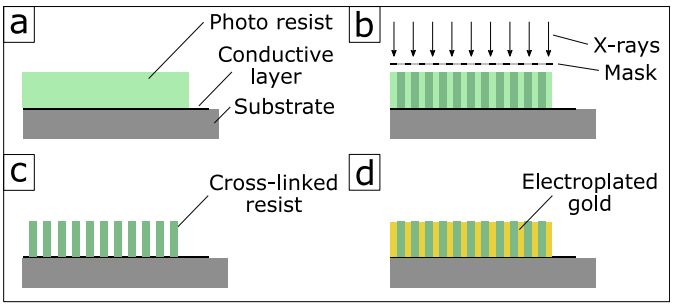

Fig. 2. Simplified illustration of the LIGA grating fabrication process, here for example with an aspect-ratio of five. a, Photo resist is applied onto the substrate. b, The resist is exposed with high-energy photons or soft X-rays passing through an absorption mask that imprints the grating layout. c, During the development step the unexposed photo resist is washed away leaving only the cross-linked resist. d, The gaps are filled via electroplating with an absorber material (e.g., gold) resulting in a lamella structure which can be used as an X-ray optical grating.

Alternative grating fabrication methods which are based on silicon etching only reach aspect-ratios of up to 80 and are restricted to silicon as substrate material due to high purity requirements [39], [40]. In contrast, the LIGA process is flexible in choice of substrate material which allows optimizing it for its mechanical or transmission properties. For example, graphite is used as a substrate material for G_2 as it combines good mechanical stability and excellent X-ray transmittance to minimize undesired attenuation behind the patient [38].

Based on this evaluation of currently available grating fabrication methods, we conclude that the finest absorption grating period in a clinical dark-field CT, i.e., the G_0 in an inverse geometry, is limited to about 4.8 µm with a height of around 200 µm. This fine grating period must be chosen to maximize interferometer sensitivity and correlation length and leads to the following periods based on a $\pi/2$ phase-shifting or absorption G_1:

$$p_0 = 4.8\ \mu\text{m} \tag{5}$$

$$p_1 = p_0 \cdot d \ / \ (L + d) \tag{6}$$

$$p_2 = p_0 \cdot d \ / \ L \tag{7}$$

To assess the performance of the system and evaluate which grating design, i.e., profile and height, is optimal, a Fresnel propagation-based simulation has been developed. It models realistic grating structures including bridges, uses the 80 kVp X-ray spectrum, and accounts for the divergent geometry of the design. It is similar to previous work by [41] and [42] and a description of the framework can be found in Appendix I.

In Fig. 3 we analyze the impact of varying G_1 structure heights and duty-cycles (ratio between lamella width and grating period) analogue to considerations by [43] for the

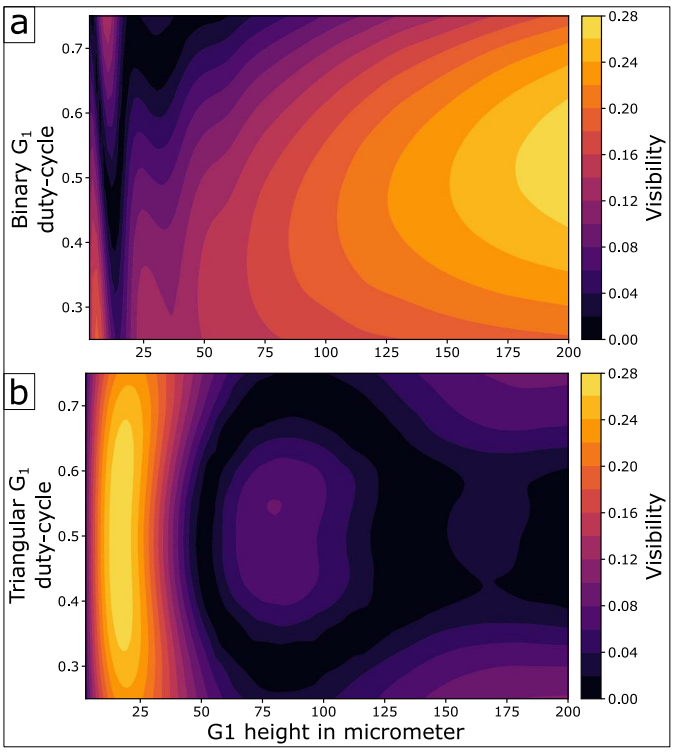

Fig. 3. Visibility simulation for binary and triangular G_1. a, For common binary phase gratings (i.e., comparably small height) only at asymmetric duty-cycles around 0.35 a slightly increased performance is expected. Significantly better results can be achieved with a binary attenuation grating with structure heights exceeding 200 μm which reaches approximately 28%. b, For the alternative triangular G_1 design also a maximum visibility around 28% is reached, however, at a more convenient height of only 18 μm. Here, G_0 and G_2 duty-cycles are 0.5 and the grating material is gold.

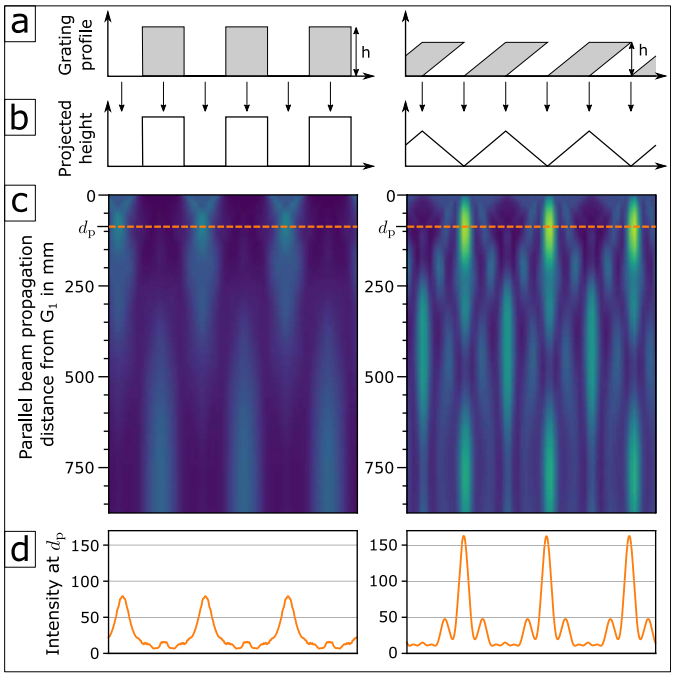

Fig. 4. Comparison of binary and triangular grating designs (left and right, respectively). a, Profiles of the binary and triangular gratings as they are fabricated (not to scale). b, Under perpendicular projection the trapezoidal profile results as a triangular profile. c, Simulated polychromatic Talbot carpets for 200 μm high binary absorption and 18 μm high triangular gratings in parallel beam (80 kVp spectrum, gold as grating material). The cone-beam geometry of our design requires a re-scaling and effectively the wave front can only propagate until d_p indicated in orange. d, Analysis of the wave front intensity at d_p which represents the G_2 position in re-scaled cone-beam geometry. It shows sharp intensity peaks for both designs and for the triangular design additional side peaks are found.

two most promising G_1 designs are shown. These simulations are performed with L and d set to 87 mm and 812 mm, respectively, no defects or bridges are included, and gold is used as the grating material for all gratings.

In Fig. 3a, the most common grating design in grating-based X-ray imaging, here referred to as binary gratings, is analyzed. It has lamella oriented perpendicular to the substrate, i.e., parallel to the beam direction, which create an alternating pattern of gaps, through which the radiation can pass unhindered, and grating bars, which attenuate and phase-shift the radiation. The common $\pi/2$ phase-shifting gratings with heights between 1-20 μm and a 0.50 duty-cycle result only in a visibility below 15%. In accordance with findings by [43] asymmetric duty-cycles in this height range lead to a slightly increased visibility, e.g., at a duty-cycle of 0.35. Only for structure heights exceeding 200 μm the visibility gets larger than 28%. Such designs no longer depend on a phase-shift in G_1 but only rely on its intensity modulation and consequently the performance has no spectral dependency. This aspect can be advantageous if the interferometer would be operated with changing kVp settings. Recently two large scale dark-field imaging setups have been developed based on such absorption G_1 designs [35], [44] and the concept is similar to edge illumination [4], [11]. A challenge in this grating design for clinical dark-field CT however is that due to the hard X-ray spectrum sufficient visibility is only achieved with high G_1 structures. As previous discussion of the grating fabrication process clarified, such high-aspect-ratio gratings are currently not favorable.

An alternative to the conventional binary grating is the triangular grating design sketched in Fig. 4a and b where the lamella are inclined to an angle α,

$$\alpha = \arctan\left(\frac{p}{2h}\right), \tag{8}$$

with p and h denoting grating period and height. This leads to a triangular grating structure under perpendicular incidence [22]. Manufacturing of such structures using the LIGA process is possible by simply tilting the mask and substrate to the angle α before the lithography step. The height of a triangular grating is the distance measured perpendicularly from the substrate to the top of the lamella as illustrated in Fig. 4a. To find the optimal height of the triangular structure the simulation results in Fig. 3b are evaluated. They reveal a performance maximum for a height of 18 μm for a duty-cycle of 0.5 which is a grating height well within the feasible range of the LIGA grating fabrication process.

These results demonstrate that for a clinical dark-field CT a triangular G_1 design is advantageous. However, there is only one experimental verification of this uncommon triangular grating structure reported in literature by [22]. Therefore,

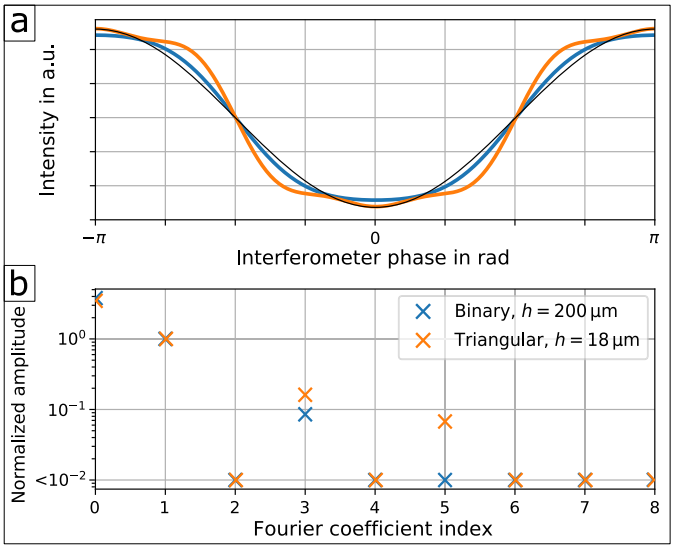

Fig. 5. Stepping curve simulation for 200 µm high binary and 18 µm high triangular G_1. All gratings are made of gold and have duty-cycles of 0.5. G_2 is 300 µm high. a, Stepping curves obtained behind a G_2 grating deviates from the expected sinusoidal shape (black). b, Fourier analysis reveals that a triangular G_1 implementation contains significant higher order contributions than a binary G_1. Data is normalized to the first Fourier coefficient.

further evaluations, e.g., of the Talbot carpet and the resulting Moiré pattern, are performed to identify potential drawbacks of this grating profile.

In Fig. 4c, polychromatic but yet perfectly coherent Talbot carpet simulations for 200 µm high binary and 18 µm high triangular G_1 are performed in parallel beam geometry. Since our design operates in a divergent beam a re-scaling from parallel to cone-beam is required [45], [46]. The orange dashed line represents the effective parallel beam propagation distance d_p which represents our proposed compact Talbot-Lau interferometer design.[1]. The results show that both designs are operated in the first fractional Talbot distance with significant contrast. Due to the polychromatic spectrum, transversal changes of the pattern are small. In the Talbot carpet simulated for the binary absorption G_1 the expected regular intensity peaks are generated. The results for the triangular grating design show sharper intensity peaks and additional small side peaks. These can also be identified in the plot of the wave front intensity in the G_2 plane in Fig. 4d. Such structures are not found in common Talbot-Lau interferometer designs, e.g., the wave front intensity simulated for the binary absorption grating does not show any side maxima.

To further analyze these additional maxima and find their impact on the Moiré pattern we simulate stepping curves for the two grating designs and evaluate them via a Fourier analysis as described in [2]. The results shown in Fig. 5a reveal that both G_1 profiles deviate from a simple sinusoidal shape, which is usually expected in Talbot-Lau interferometry. For the binary G_1 the deviation is small but increases significantly in the triangular G_1 design. These deviations can be identified as a higher order sinusoidal signal by the Fourier analysis, shown in Fig. 5b, where the third and fifth Fourier coefficient is increased compared to the stepping-curve obtained from an absorption G_1 setup. When a G_0 is added to the interferometer the convolution with the extended slit sources leads to a decrease of the higher orders. Nevertheless, for a triangular G_1 they remain higher than for a binary G_1.

This analysis reveals that when working with triangular G_1 gratings the higher Fourier coefficients do not decay as fast as at common binary G_1 setups. Conventional data processing approaches in Talbot-Lau interferometry usually only consider the first order because of the rapid decay [47] but this might not be sufficient for a setup with a triangular G_1 grating. While Fourier processing, as defined in [2], can efficiently separate the higher order contributions, other methods, e.g., model-based processing approaches, can easily run into artifacts because the first order sinusoidal model of the stepping curve no longer applies.

We conclude that triangular G_1 gratings are an advantageous choice for a clinical dark-field CT implementation because they achieve good visibility results with small grating structure heights of only around 18 µm. The higher order contributions in the fringe pattern can easily be considered in the data model and have only a minimal effect on the system visibility, consequently we see no drawbacks. The alternative over 200 µm high absorption grating G_1 design performs similarly well, but is more difficult to fabricate and absorbs about 50% of the incident X-ray flux.

In terms of patient dose, there is no difference between the triangular and absorption G_1 implementation because this grating is positioned before the patient. Nevertheless, it must be considered that X-ray tube power is limited and must be increased to compensate for the absorbed flux in the gratings to maintain a sufficient intensity on the detector. The triangular G_1 design is in this regard again favorable because it absorbs only 4.2% of the incident flux if implemented as a nickle grating or up to 12.5% when made of gold. Simulations with a purely phase-shifting material (i.e., neglecting the attenuation property of gold) revealed that in the triangular grating design solely the phase-shift generates the Moiré pattern and consequently the absorption is an undesired side effect. To generate this phase-shift with nickle a structure height of 42 µm is required, in contrast, with gold already 18 µm are enough. For the prototype dark-field CT implementation the triangular G_1 design with a gold grating has been chosen favoring simpler grating fabrication as a compromise between small height and acceptable absorption in the grating.

For G_1 in either design a duty-cycle of 0.50 is optimal (see Fig. 3), in contrast, for G_0 and G_2 the following evaluation reveals optimization potential by selecting an asymmetric duty-cycle. These two absorption gratings have significant impact on the beam intensity reaching the detector as larger duty-cycles lead to more absorption in the gratings and subsequently not being used for imaging. While noise in the attenuation images is purely intensity dependent, in the dark-field channel noise level σ is,

$$\sigma \propto \left(V\sqrt{I}\right)^{-1}, \tag{9}$$

depending on the system visibility V and measured intensity I [48]. Consequently, a trade-off between visibility,

[1]Based on the Fresnel scaling theorem $d_p = d \cdot L/T$ [45].

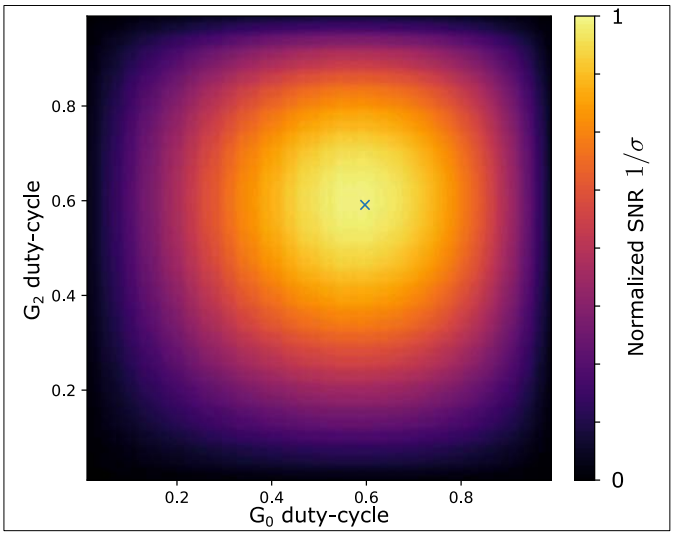

Fig. 6. Duty-cycle optimization of G_0 and G_2 with structure heights 200 μm and 300 μm, respectively. Based on (9), the simulation shows the best signal-to-noise ratio (SNR) for a duty-cycle of 0.60 and 0.59 for G_0 and G_2, respectively. A triangular G_1 with duty-cycle 0.5 has been used for this simulation.

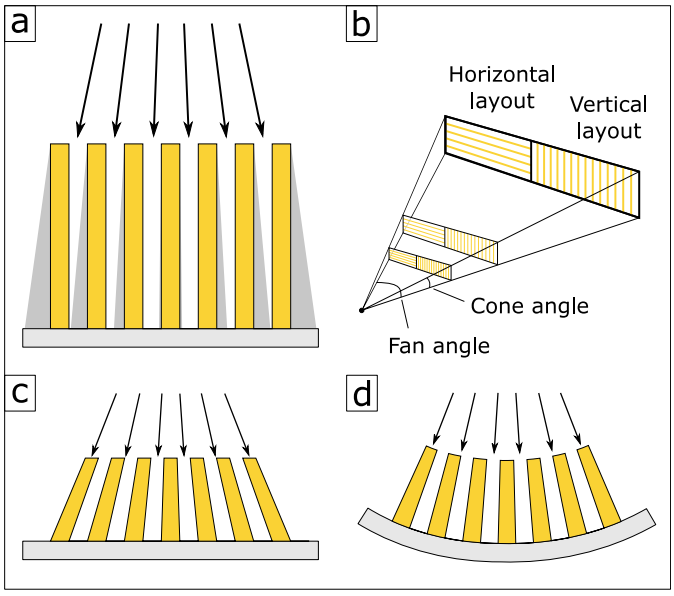

Fig. 7. Illustration of the shadowing problem and two solutions. a, Cross-section of a grating. Due to the divergent beam and high aspect-ratio, grating structures cause shadowing perpendicular to the grating lines. b, Two layout options are considered, namely vertical and horizontal layout. c, A grating design with divergent lamella layout on a flat substrate can eliminate the shadowing problem. Just recently the first gratings of this type have been demonstrated as it is difficult to fabricate an individual inclination angle for each lamella. d, A conventional grating, i.e., with parallel structures as depicted in a, can be bent to focus each grating slit into the source spot countering the shadowing artifact but requiring a flexible substrate.

which increases with larger duty-cycles, and intensity, which decreases with larger duty-cycles, must be found.

The simulation results for different G_0 and G_2 duty-cycles, shown in Fig. 6, based on (9) reveal that for our proposed design the best dark-field signal-to-noise ratio is found for duty-cycles of 0.60 and 0.59 for G_0 and G_2, respectively. This simulation considers G_0 and G_2 with a structure height of 200 μm and 300 μm, respectively.

For our prototype dark-field CT system we conclude on G_0 and G_2 duty-cycles of 0.6 and 0.56, respectively. The choice of a lower nominal G_2 duty-cycle than suggested by the simulation takes fabrication variations of the duty-cycle into account. This ensures that deviations do not lead to an increase of patient dose without an increase of the signal-to-noise ratio.

As discussed earlier, also the G_1 has a significant impact on the X-ray flux, particularly, if an absorption G_1 is implemented. Based on the signal-to-noise ratio evaluation a comparison of the triangular and the absorption G_1 design is possible. It yields a better performance for the triangular design because this G_1 stops less X-ray flux and thus leads to an approximately 30% higher signal-to-noise ratio than an absorption G_1 design. This reveals an additional argument for use of a triangular G_1 design in our clinical dark-field CT prototype as it maximizes the imaging performance for the dark-field channel.

V. Adaptation to Fan-Beam Geometry

Since clinical CT systems cover a large field of view in a compact geometry, the design of the gantry is adapted to this divergent beam geometry, for example, by having a curved detector. Space within the gantry is confined and to maximize interferometer sensitivity the distance between the gratings must be maximized and consequently also the interferometer must be adapted to this curved geometry. To achieve this the gratings must be bent along the fan angle to a cylindrical interferometer design. Another advantage of this design is that the propagation distance is independent of the fan angle, since for all ray paths the distances between the gratings are identical. This ensures consistent performance since, e.g., the sensitivity is distance dependent.

Besides this space and geometry related issue, so-called shadowing in high aspect-ratio gratings is a problem which also must be avoided: It occurs in a divergent beam where off-center rays, which traverse the grating at a non-perpendicular angle, are partially absorbed by the lamella and cause intensity and visibility loss. This effect is illustrated in Fig. 7a and occurs only perpendicular to the grating lines and thus has a directional dependency. Since clinical CT systems have, compared to laboratory systems, a large beam divergence with, e.g., 2.1° and 46° of cone and fan opening at our prototype system, respectively, suppression of the shadowing artifact is a crucial design challenge and different solutions are evaluated.

Fig. 7b illustrates the vertical and the horizontal grating layout, which only differ in the orientation of the grating lines. As the cone angle in a clinical CT is comparably small, it is an option to orientate the grating lines along the fan angles and thus have a horizontal grating design. This results in no shadowing along the fan angles, however, shadowing in cone direction remains because of the high aspect-ratio.[2] To compensate for the remaining shadowing in cone direction a divergent lamella structure, which focuses each grating gap

[2]Note that the acceptance angle (angle of diagonal transmission through lamella and slit) of G_0 with period 4.8 μm and height 200 μm is only 1.4°.

onto the focal spot, can solve this problem. Fig. 7c illustrates this approach, which inclines the lamella individually and can eliminate shadowing. Recently, first gratings of this type have been demonstrated in silicon substrates [40] and via an adapted LIGA process [49].

Alternatively, additional bending of the grating lines along the cone angle is an option. As shown in Fig. 7d, this aligns the grating slits to focus into the X-ray source spot and can avoid shadowing. However, in combination with the mandatory bending along the fan this would here result in a spherically bent grating. Cylindrically bent gratings are common, in contrast, spherical bending has not yet been demonstrated and is assumed to be difficult to implement and adjust, particularly in a compact design as it is required for our clinical dark-field CT prototype. We therefore find the alternative layout which uses vertical grating lines advantageous. Since bending along the fan angle is mandatory to use all available space in the gantry, it simultaneously also focuses the grating slits into the focal spot and avoids shadowing. Along the cone angle, there is no shadowing because of the direction dependence of the effect. Consequently, cylindrically bent gratings are sufficient and can be implemented only requiring a flexible substrate [50].

We evaluated the mechanical properties of different grating substrate materials and thicknesses, and conclude that polyimide and graphite substrates with 600 µm thickness or thinner work well for bending radii of 100 mm and larger. Tests with 250 µm thick silicon substrates for the G_1 with a bending radius around 180 mm were successful in terms of material flexibility but turned out to be unreliable in application as already small defects and stresses caused shattering of the substrate. To avoid defect formation in the grating structure, bending must be performed with the structured surface towards the source, which leads to a compression of the structures without any defects.

Following from the previous discussion for the clinical dark-field CT prototype, a cylindrically bent grating setup with a vertical grating layout is used as illustrated in Fig. 8. For G_0 a graphite substrate with 600 µm thickness and for G_1 a 500 µm thick polyimide substrate ensure sufficient flexibility. Since both these gratings have only a small and slot-like active area in the beam path, the mounts can have a large contact surface along the long sides of the slot and the support-free distance across the slot is only 15 mm. This allows to efficiently stabilize the gratings against deformations from, e.g., centrifugal forces or vibrations. In contrast, the G_2 is positioned further downstream and must cover a much larger area without support by the mount. Here we use 1 mm thick graphite substrates which are suitable for the large bending radius of about one meter and provide high stability against deformations. These substrate materials and thicknesses have proven to be long-term stable based on the oldest G_2 tiles being implemented since 2017 and not exhibiting any aging from radiation, thermal, or mechanical stress. In terms of X-ray transmission, all these substrates combined absorb 6% of the incident flux, which is negligible compared to the two absorption gratings which each stop over 50% of the radiation.

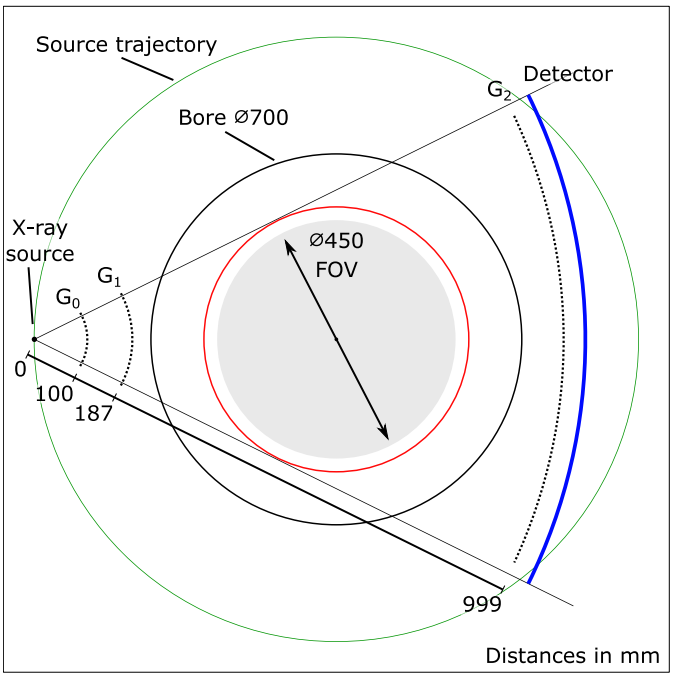

Fig. 8. Cylindrical dark-field CT design with an inverse Talbot-Lau interferometer consisting of bent gratings. The layout is adapted to the curved detector shape, which maximizes the length of the interferometer and thereby maintains the original bore diameter (70 cm) of the clinical CT. In our dark-field CT prototype, the field of view is limited to the gray area with a diameter of 45 cm, which is slightly smaller than the conventional field of view sketched in red (50 cm). With only one large grating behind the patient and carefully selected grating specifications, the setup can be built with state-of-the-art grating fabrication technology.

VI. Grating Parameter Optimization

Besides the realization of a grating-based interferometer in the clinical CT gantry, dark-field CT is also a product of processing the obtained data and its reconstruction. In the clinical environment, typically data from only a single rotation can be used for a reconstruction to minimize patient motion artifacts and excessive scan duration. The acquisition is continuous with integration periods in the sub-millisecond range which makes stepping-based acquisition [51], the most common approach in grating-based imaging, not feasible because fast repositioning of the grating is difficult at the short timescales. We therefore pursue two alternative processing and reconstruction methods and optimize the interferometer design accordingly.

The first approach is based on the *sliding window* signal extraction, which is a robust and fast method [52]. Several consecutive projections from different rotation positions are interpreted as a conventional stationary stepping and processed accordingly. Depending on the window-size, i.e., the number of combined projections, the reconstruction becomes blurred, hence, small window-sizes are advantageous. This method has no special requirements to the grating adjustment except that the interferometer phase must vary between the individual projections. At laboratory setups this is achieved by stepping one grating perpendicular to its grating lines, but this approach is currently not feasible for continuous image acquisition as used in clinical CT. Instead, the variation of the interferometer phase by intrinsic deformations of the CT gantry during rotation or

from vibrations is utilized. Work by [53] revealed that the displacement between two neighboring projections must be a sufficiently small fraction of the grating periods because the interferometer performance otherwise decreases quickly. This motivates a rigid design of the setup to keep the vibrations and deformations to a minimum and add displacements, e.g., with a motorized solution, if required. The intrinsic vibrations of the system in combination with the high frame-rate of the detector are sufficient to allow sliding window signal extraction without any additional perturbation.

The second processing approach is the *intensity based statistical iterative reconstruction* (IBSIR), which directly reconstructs the different modalities from the acquired data without any intermediate signal extraction [54], [55]. This algorithm is more complex than sliding window and requires a slightly de-tuned fringe pattern of the interferometer for better sampling in Radon space in order to circumvent artifacts. To establish the required phase gradient, i.e., a Moiré-fringe pattern with a given period, one of the gratings can be moved some by millimeters along the beam axis [56] causing the required de-tuning. However, due to the space limitation in a clinical CT the travel range along the beam axis is limited. The design of the grating periods therefore already includes the de-tuning for a target geometry with $T = 899$ mm in our dark-field CT prototype. During installation into the gantry, the position along the beam-axis then only requires some fine-tuning of G_2 with specialized mechanics and is locked afterwards.

A consequence of this approach is that in the process of de-tuning the Moiré fringe pattern some visibility is sacrificed because of the large detector pixels in a clinical CT (around 1 mm $\times$ 1 mm) which can no longer resolve the full contrast of the de-tuned Moiré pattern. This is a fundamental problem when using an analyzer grating, i.e., G_2, with a coarse detector resolution and must be considered during system design to avoid unexpected visibility loss. We integrated this aspect into our wave-optical simulation by modeling the physical pixel size of the system, and could validate the results in experiments at a micro-focus X-ray tube with a 100 µm source spot. The experiments are in accordance with our simulations, as shown in Fig. 9b, and demonstrate that an increase of fringes per pixel goes along with a loss of visibility. The results also show that our design requires a G_2 de-tuning of approximately 4 mm from the tuned design, i.e., the state without any Moiré fringes, to have the optimal phase gradient of 0.1 fringes per pixel for IBSIR [54]. For this setting the visibility is still high but would quickly drop if a denser fringe pattern was required.

Another important aspect is the large X-ray source spot in a clinical CT, which usually is 0.9 mm or larger in width specified according to IEC 60336 [57]. Specifically, we use the small focal spot of the iCT, which is 0.6 $\times$ 0.7. This translates according to IEC 60336 to a width of 0.9 mm and a height of 1.1 mm. This norm, however, states the dimensions of the focal spot only for the view through the iso-center, i.e, where fan and cone angle are zero. The effective source size increases into the millimeter range for the far-out fan angles because the X-ray source spot is a rectangular area on an inclined anode

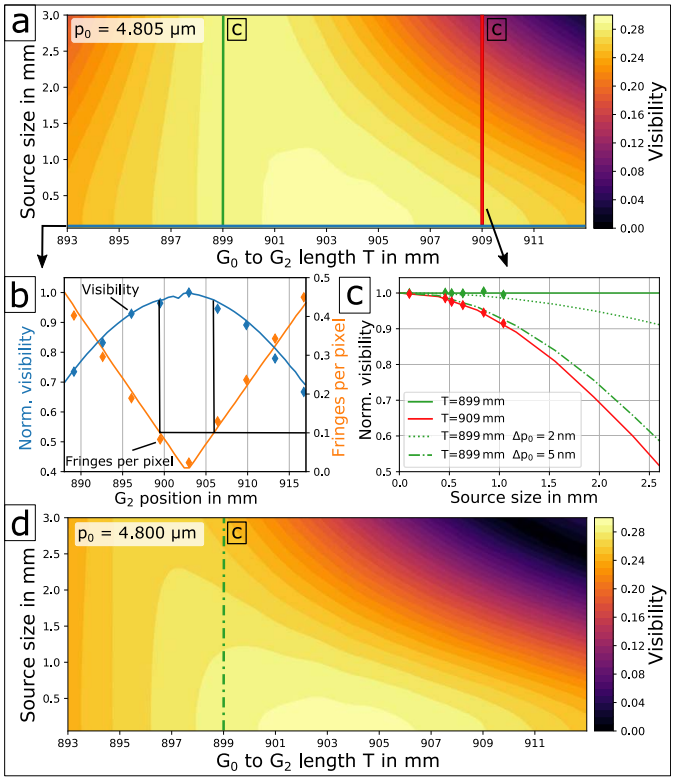

Fig. 9. Performance dependencies on G_0 period, G_2 position, and focal spot size. a, Simulation demonstrates a constant visibility across a large range of source sizes at the design length $T = 899$ mm. b, Due to the extended physical pixel size some visibility is sacrificed to establish the 0.1 fringes per pixel Moiré pattern at the design length $T = 899$ mm. c, The impact of the source size on the system visibility depends strongly on geometry and grating periods. d, A small periodicity mismatch of only 5 nm in combination with a large focal spot leads to a significant visibility loss. The ♦ represent values obtained at a laboratory setup.

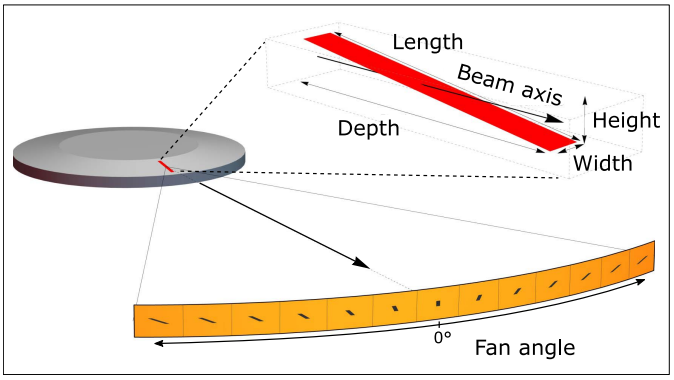

Fig. 10. Source spot shape variation under different fan angles. Due to the elongated physical source spot (red) on the rotating anode target, the shape of the focal spot changes significantly towards the outer fan angles.

surface onto which the electrons are accelerated [58]. At our dark-field CT prototype, the 8° anode surface inclination leads to a width variation between 0.9 and 3.9 mm for the central fan angle at 0° and the outermost fan angle at 23°, respectively. This behavior is illustrated in Fig. 10 by projecting the physical source spot into the detector plane for several fan angles.

For conventional CT systems the change in focal spot size implies that the spatial resolution that can be achieved falls with increasing distance to the iso-center, which is

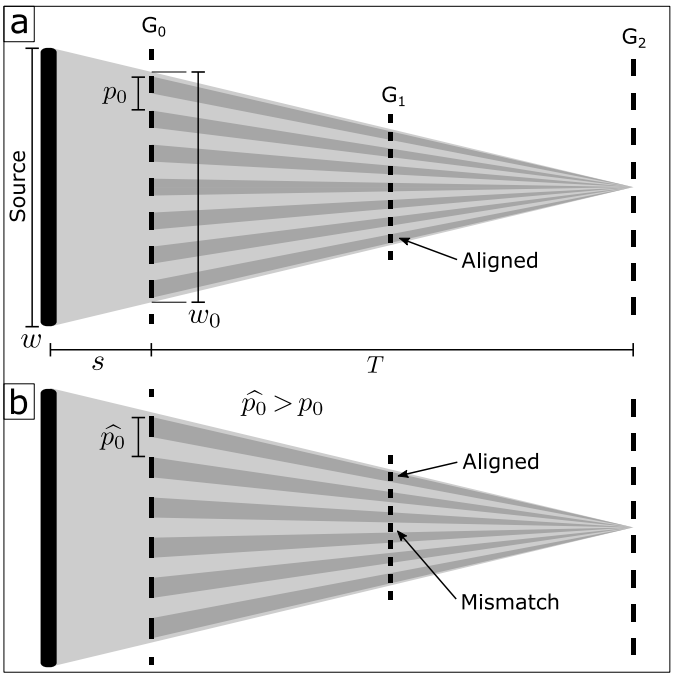

Fig. 11. Illustration how an extended source size tightens period tolerances. a, Only when the grating periods are precisely matched, the constellation of G_0 slits interlace constructively in the G_2 plane. b, A wrong grating period, e.g., here $\widehat{p_0}$ in G_0, leads to performance losses as the interference patterns no longer coincide.

well known and accepted. For a Talbot-Lau interferometer, however, an additional effect is that the design becomes more sensitive to grating period tolerances and positioning errors. We can derive this by analysis of all ray paths which contribute to a sampling point in the G_2 plane and start from the surface of the extended X-ray source spot. Ideally, the transmitted G_0 and G_1 patterns have the same number of periods and thus the coherence condition holds as illustrated in Fig. 11a. For example, the active G_0 area w_0 in the beam path to a G_2 sampling point is given as

$$w_0 = w\frac{T}{s+T}\,, \tag{10}$$

where w is the projected source width, leading to a number of contributing G_0 slits

$$n_{\text{bars}} = \frac{w_0}{p_0}\,, \tag{11}$$

where p_0 is the G_0 period. The variables s and T here denote the distances between source to G_0 and G_0 to G_2 as indicated in Fig. 11a.

In a clinical CT geometry, where the G_0 is close to the source and the spot size is large, the number of G_0 slits can easily be in the hundreds. Consequently, with increasing number of contributing slits already a small period-deviation adds up to an increasing misalignment with the G_1 pattern as illustrated in Fig. 11b. The first performance minimum is reached for a G_0 with period $\widehat{p_0}$ when the number of contributing G_0 slits deviates by $i = \pm 1$, i.e., one grating period,

$$n_{\text{bars}} + i = \frac{w_0}{\widehat{p_0}}\,, \tag{12}$$

into which (11) can be inserted and reshaped to,

$$\widehat{p_0} = \frac{1}{1/p_0 + i/w_0}\,. \tag{13}$$

For our prototype dark-field CT this yields, with $p_0 = 4.805$ µm and a maximum source size $w_0 = 3.5$ mm (with s, T, and w being 100, 899 and 3.9 mm, respectively), that the first performance minimum is reached when G_0 deviates to a period $\widehat{p_0} = 4.812$ µm or $\widehat{p_0} = 4.798$ µm. This means, a G_0 period deviation of only 7 nm can results in a total loss of interferometer performance for the outermost fan angles, i.e., where the projected source spot is approximately 3.9 mm wide. For the central beam through the iso-center the constraint is more relaxed and would lead to a total performance loss for a G_0 period deviation of about 30 nm because there the source spot is approximately 0.9 mm wide.

To consider this effect in our wave-optical simulation, we implemented the projected source profile properties as a multi-slit source based on the X-ray source spot definition in [57]. More information on the simulation framework can be found in the Appendix I. Based on this extension it is possible to analyze the interferometer design and optimize it to have maximum visibility for an interferometer state with 0.1 fringes per pixel at a design length $T = 899$ mm. In Fig. 9a, the simulations of different source sizes and G_2 displacements demonstrate the significant impact of the large source size once a parameter deviates from its nominal value. Experimental measurements with a 4.805 µm period G_0 at an X-ray source with variable source spot size could verify the simulated behavior as shown in Fig. 9c. For two G_2 positions the interferometer visibility has been measured and is compared to the simulation results. The obtained values are normalization to compensate for visibility loss caused by grating defects and bridges, which are not considered in this simulation. The scan range is limited by the laboratory X-ray source (XWT-160-SE, X-ray WorX, Germany) which can only be tuned to focus sizes between 0.1 and 1.1 mm.

To illustrate the system's sensitivity to grating period deviations, in Fig. 9d, a simulation with a by 5 nm different G_0 period is shown. In contrast to the simulation in Fig. 9a, the mismatch of the interferometer grating periods leads to significant visibility losses for the target design with $T = 899$ mm. In Fig. 9c the respective line plot is shown for the depicted 5 nm deviation.

Based on these results we find that tight tolerances on the grating period are required to avoid performance loss in combination with the large source spot of a CT machine. Previous calculations found a 7 nm deviation to be fatal for the system performance, and we suggest a 2 nm tolerance on the grating periods of this design. This will limit the potential relative visibility loss due to the extended focal spots to 10% for source sizes until about 2.6 mm width, as shown in Fig. 9c based on corresponding simulation results.

To achieve this tight tolerance multiple potential sources of grating period distortion, such as several steps in the fabrication process, mechanical stress during installation, or thermal expansion, must be considered and kept to a minimum. In our dark-field CT prototype, deviations are compensated by

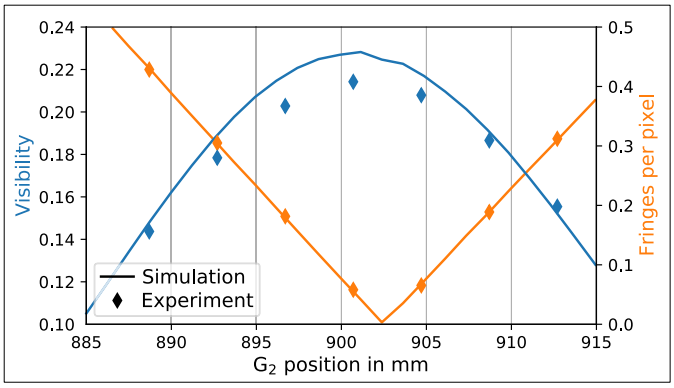

Fig. 12. Adjustable interferometer performance. The optimized interferometer design is simulated here for a 1.1 mm large source spot according to the parameters listed in Table I. Reference measurements at a laboratory setup confirm that the design results in the demanded period of 0.1 Moiré fringes per pixel. The measured visibility follows the same trend as the simulated ones, but do not fully reach the same height. This is probably caused by remaining grating imperfections which are not yet sufficiently modeled by the simulation.

TABLE I
PROPOSED DESIGN PARAMETERS

	G_0	G_1	G_2
Distance to source [mm]	100	187	999
Period [µm]	4.805	4.338	45.0
Height [µm]	$\geq$ 200	18	$\geq$ 300
Bridge fraction	10%	10%	1%
Duty-cycle	0.60	0.50	0.56
Grating profile	Binary	Triangular	Binary
Grating material	Gold	Gold	Gold
Substrate material	Graphite	Polyimide	Graphite
Substrate thickness [µm]	600	500	1000

adjustment of the G_2 position along the beam path and by an evaluation and quality check of all interferometer components in a dedicated laboratory setup.

Considering the spatial constraints in the CT gantry, the size of the detector pixels and projected X-ray source spot, and the requirements for the data processing we optimized the setup parameters with the extended wave-optical simulation for best visibility and for being adjustable in the gantry. The resulting design parameters are tabulated in Table I and yield an interferometer with the demanded 0.1 Moiré fringes per pixel in the target interferometer length of $T = 899$ mm. The simulation results of the optimized design plotted in Fig. 12 are in agreement with experimental measurements at different G_2 positions along the beam path. The design can be fine adjusted inside the gantry by moving the G_2 position along the beam axis until the correct number of fringes is measured on the detector. In contrast, the visibility cannot be optimized in this way and has its maximum close to the 899 mm position. The visibility is only slightly overestimated by the simulation, presumably because some remaining grating imperfections are not yet sufficiently modeled by the simulation.

VII. CONCLUSION

In this work we discussed the considerations and design decisions for development of a clinical dark-field CT which recently led to the prototype system published in [21]. We analyzed the possible interferometer geometries and concluded on the inverse geometry as it convinces with smaller grating sizes, more compact package, and a lower patient dose. A wave-optical simulation-based evaluation of the two most promising G_1 profiles revealed that currently a triangular grating is advantageous but can come with higher order contributions in the Moiré pattern. Since these are small and can be included into the data model this aspect poses no problem.

To compensate shadowing from the divergent beam, we concluded that a vertical grating layout which is cylindrically bent to the source spot is currently the best solution. The promising alternative, the horizontal layout, is not yet feasible at the required dimensions and aspect-ratios. An evaluation of the CT X-ray source spot revealed that for large fan angles also the effective source width becomes large and can degrade the interferometer performance. This impact of a large source spot on a Talbot-Lau interferometer has been analyzed in detail and could be related to a significant sensitivity to grating period deviations. For the presented design, we found that tolerances of the grating periods must lie within 2 nm to avoid visibility loss due to the large source spot. With an extended simulation framework we then optimized the grating parameters for the data processing approaches which are applicable at the continuous acquisition of a clinical CT, i.e., sliding window signal extraction and IBSIR.

Based on this evaluation, the design parameters as stated in Table I have been derived and the resulting design yields a correlation length of 0.22 µm. While this cannot reach the challenging correlation length criterion demanded by [16] (this would require a 1.0 µm fine G_0 which is currently not feasible to fabricate), this leaves the proposed dark-field CT design at around half the sensitivity of the dark-field chest radiography system [20] which is operating successfully in clinical routine. We are confident that the tomographic reconstruction allows us to compensate for this drawback, as the volume reconstruction allows us to work with advanced processing and filtering approaches not applicable in radiographic imaging. Recently, initial results including first reconstructions of human scale phantoms have been published in [21]. The successful realization of this prototype system is a significant step towards making dark-field CT available for clinical practice. Nevertheless, our work reveals several potential improvements in future designs, particularly concerning the issues with the large X-ray source size and the related tight tolerances for the grating periods.

APPENDIX I
SIMULATION FRAMEWORK

For a comprehensive analysis and optimization of different Talbot-Lau interferometer designs, we developed a numerical wave-optical simulation tool which is based on Fresnel propagation of the various interferometer components. It is based on previous work by [41] or [42] and has recently been briefly described in [21].

As demonstrated in this work the simulation tool allows us to run large parameter studies while simultaneously considering a large variety of realistic system properties which gives

us realistic performance results. This helps when correlating experimental results with the simulation as the common overestimation in simulation results is minimized. For example, the implementation of the gratings can be freely parameterized for the period, height, duty-cycle, bridge fraction, bending radius and grating profile. Furthermore, the material and height of the substrate, the grating lamella, and the resist matrix are considered.

To include spectral effects, the X-ray power spectrum of the clinical source is used. Additional filtration, e.g., representing a patient, the grating substrates, the grating structures, and the detector efficiency, can also be applied to this spectrum. The required material interaction coefficients have been obtained from the xraylib library [59].

To make a polychromatic simulation, the power spectrum of the X-ray tube is separated in multiple energy bins. The monochromatic Fresnel propagation-based simulation is run individually for each bin, and the resulting intensities reaching the detector plane are then integrated according to the detector specifications.

Each of those mono-energetic propagation simulations starts as a complex valued plane wave front in front of G_1. Based on projection approximation, the structures of G_1 are applied to the wavefront inducing the characteristic attenuation and phase shifts. Afterwards, a free space propagation into the G_2 plane follows based on Fresnel propagation and the Fourier scaling theorem [45]. Here, the complex wave front is converted to its intensity, referred to as intensity wave front, by calculating the absolute square of the complex wave front. In the next step, the G_0 is applied to the wave front and this step also includes the effect of an extended source spot. This is achieved by first deriving the active area of G_0 similar to the illustration in Fig. 11, e.g., by projecting the source power profile into a G_2 sampling point. Then the G_0 transmittance of the identified grating area is calculated based on its attenuation properties, which yields the periodic slit pattern from which a G_2 sampling point is illuminated. This G_0 transmittance is then projected into the G_2 plane over the G_1 plane. At this point the propagated wave front intensity, the G_2 structure, and the projected G_0 transmittance should have the same periodicity for simulation of a Talbot-Lau interferometer. To apply the G_0 and the source profile the projected intensity wave front is convolved with the projected G_0 transmittance, which leads to a blurring, and generates the fine interference pattern which has a similar period as the G_2 pattern. As a final step, the G_2 attenuation is applied to the intensity wave front and the result is binned according to the physical pixel size of the detector. This last step is repeated several times for different displacements of the G_2 structure over one G_2 period to obtain a stepping curve on the detector pixels.

Once this simulation has been performed for all energy bins, the results in the detector pixels are weighted with the power spectrum and summed up. By processing the stepping curve, e.g., with Fourier processing [2], the intensity and interferometer visibility and phase can be extracted. To determine the density of Moiré fringes on the detector a row of several neighboring detector pixels must be simulated to calculate the resulting phase gradient which then can be converted to Moiré fringes per mm.

The simulation can be stopped at any point to evaluate, e.g., the formation of the Talbot carpet as shown in Fig. 4 or the stepping curves as in Fig. 5.

Acknowledgment

The authors would like to thank Julia Herzen, Daniela Pfeiffer, Alexander Fingerle, Ernst Rummeny, Pascal Meyer, Jürgen Mohr, Maximilian von Teuffenbach, Amanda Pleier, Michael Heider, Sven Prevrhal, Thomas Reichel, Ami Altman, and Shlomo Gotman for their help, support, and dedication to launch this complex project.

References

[1] T. Ai *et al.*, "Correlation of chest CT and RT-PCR testing for coronavirus disease 2019 (COVID-19) in China: A report of 1014 cases," *Radiology*, vol. 296, pp. E32–E40, Aug. 2020.

[2] F. Pfeiffer *et al.*, "Hard-X-ray dark-field imaging using a grating interferometer," *Nature Mater.*, vol. 7, no. 2, pp. 134–137, 2008.

[3] Z.-F. Huang *et al.*, "Alternative method for differential phase-contrast imaging with weakly coherent hard x rays," *Phys. Rev. A, Gen. Phys.*, vol. 79, Jan. 2009, Art. no. 013815.

[4] P. Modregger, T. P. Cremona, C. Benarafa, J. C. Schittny, A. Olivo, and M. Endrizzi, "Small angle X-ray scattering with edge-illumination," *Sci. Rep.*, vol. 6, no. 1, p. 30940, Aug. 2016.

[5] F. Arfelli, A. Astolfo, L. Rigon, and R. H. Menk, "A Gaussian extension for diffraction enhanced imaging," *Sci. Rep.*, vol. 8, no. 1, p. 362, Dec. 2018.

[6] M.-C. Zdora, "State of the art of X-ray speckle-based phase-contrast and dark-field imaging," *J. Imag.*, vol. 4, p. 60, Apr. 2018.

[7] T. E. Gureyev *et al.*, "Dark-field signal extraction in propagation-based phase-contrast imaging," *Phys. Med. Biol.*, vol. 65, Nov. 2020, Art. no. 215029.

[8] F. Pfeiffer, O. Bunk, C. Kottler, and C. David, "Tomographic reconstruction of three-dimensional objects from hard X-ray differential phase contrast projection images," *Nucl. Instrum. Methods Phys. Res. Sect. A, Accel., Spectrometers, Detectors Associated Equip.*, vol. 580, pp. 925–928, Oct. 2007.

[9] T. Weitkamp, C. David, C. Kottler, O. Bunk, and F. Pfeiffer, "Tomography with grating interferometers at low-brilliance sources," *Proc. SPIE*, vol. 6318, Sep. 2006, Art. no. 63180S.

[10] M. Bech, O. Bunk, T. Donath, R. Feidenhans'l, C. David, and F. Pfeiffer, "Quantitative X-ray dark-field computed tomography," *Phys. Med. Biol.*, vol. 55, pp. 5529–5539, Aug. 2010.

[11] M. Endrizzi *et al.*, "Hard X-ray dark-field imaging with incoherent sample illumination," *Appl. Phys. Lett.*, vol. 104, Jan. 2014, Art. no. 024106.

[12] S. Schleede *et al.*, "Emphysema diagnosis using X-ray dark-field imaging at a laser-driven compact synchrotron light source," *Proc. Nat. Acad. Sci. USA*, vol. 109, no. 44, pp. 17880–17885, 2012.

[13] K. Hellbach *et al.*, "In vivo dark-field radiography for early diagnosis and staging of Pulmonary Emphysema," *Investigative Radiol.*, vol. 50, no. 7, pp. 430–435, 2015.

[14] A. Yaroshenko *et al.*, "Improved *in vivo* assessment of pulmonary fibrosis in mice using X-ray dark-field radiography," *Sci. Rep.*, vol. 5, p. 17492, Dec. 2015.

[15] K. Scherer *et al.*, "X-ray dark-field radiography-*in-vivo* diagnosis of lung cancer in mice," *Sci. Rep.*, vol. 7, p. 402, Mar. 2017.

[16] V. Ludwig *et al.*, "Exploration of different X-ray Talbot-Lau setups for dark-field lung imaging examined in a porcine lung," *Phys. Med. Biol.*, vol. 64, no. 6, Mar. 2019, Art. no. 065013.

[17] F. G. Meinel *et al.*, "Improved diagnosis of pulmonary emphysema using *in vivo* dark-field radiography," *Investigative Radiol.*, vol. 49, no. 10, pp. 653–658, Oct. 2014.

[18] A. Velroyen *et al.*, "Grating-based X-ray dark-field computed tomography of living mice," *EBioMedicine*, vol. 2, no. 10, pp. 1500–1506, Oct. 2015.

[19] A. Tapfer *et al.*, "Development of a prototype gantry system for preclinical X-ray phase-contrast computed tomography," *Med. Phys.*, vol. 38, no. 11, pp. 5910–5915, Oct. 2011.

[20] K. Willer *et al.*, "X-ray dark-field chest imaging for detection and quantification of emphysema in patients with chronic obstructive pulmonary disease: A diagnostic accuracy study," *Lancet Digit. Health*, vol. 3, no. 11, pp. e733–e744, Nov. 2021.

[21] M. Viermetz *et al.*, "Dark-field computed tomography reaches the human scale," *Proc. Nat. Acad. Sci. USA*, vol. 119, no. 8, Feb. 2022, Art. no. e2118799119.

[22] A. Yaroshenko *et al.*, "Non-binary phase gratings for X-ray imaging with a compact Talbot interferometer," *Opt. Exp.*, vol. 22, no. 1, pp. 547–556, 2014.

[23] D. Devitt, "Radial air bearings help CT scanners see into your heart," *Des. World Mag.* pp. 62–64, Dec. 2009.

[24] T. Donath *et al.*, "Inverse geometry for grating-based X-ray phase-contrast imaging," *J. Appl. Phys.*, vol. 106, no. 5, Sep. 2009, Art. no. 054703.

[25] H. Miao *et al.*, "Motionless phase stepping in X-ray phase contrast imaging with a compact source," *Proc. Nat. Acad. Sci. USA*, vol. 110, no. 48, pp. 19268–19272, Nov. 2013.

[26] L. Birnbacher *et al.*, "Experimental realisation of high-sensitivity laboratory X-ray grating-based phase-contrast computed tomography," *Sci. Rep.*, vol. 6, p. 24022, Apr. 2016.

[27] F. Schaff, F. Prade, Y. Sharma, M. Bech, and F. Pfeiffer, "Non-iterative directional dark-field tomography," *Sci. Rep.*, vol. 7, pp. 1–9, Jun. 2017.

[28] E. M. Braig *et al.*, "Simultaneous wood and metal particle detection on dark-field radiography," *Eur. Radiol. Experim.*, vol. 2, pp. 1–7, Dec. 2018.

[29] T. J. Schröter *et al.*, "Large field-of-view tiled grating structures for X-ray phase-contrast imaging," *Rev. Sci. Instrum.*, vol. 88, Jan. 2017, Art. no. 015104.

[30] T. G. Flohr, K. Stierstorfer, C Süß, B. Schmidt, A. N. Primak, and C. H. McCollough, "Novel ultrahigh resolution data acquisition and image reconstruction for multi-detector row CT," *Med. Phys.*, vol. 34, pp. 1712–1723, May 2007.

[31] U. van Stevendaal, Z. Wang, T. Köhler, G. Martens, M. Stampanoni, and E. Roessl, "Reconstruction method incorporating the object-position dependence of visibility loss in dark-field imaging," *Proc. SPIE*, vol. 8668, Mar. 2013, Art. no. 86680Z.

[32] W. Yashiro, Y. Terui, K. Kawabata, and A. Momose, "On the origin of visibility contrast in X-ray Talbot interferometry," *Opt. Exp.*, vol. 18, p. 16890, Aug. 2010.

[33] M. Strobl, "General solution for quantitative dark-field contrast imaging with grating interferometers," *Sci. Rep.*, vol. 4, p. 7243, Nov. 2014.

[34] S. K. Lynch *et al.*, "Interpretation of dark-field contrast and particle-size selectivity in grating interferometers," *Appl. Opt.*, vol. 50, pp. 4310–4319, Aug. 2011.

[35] L. B. Gromann *et al.*, "*In-vivo* X-ray dark-field chest radiography of a pig," *Sci. Rep.*, vol. 7, p. 4807, Jul. 2017.

[36] A. P. Sauter *et al.*, "Optimization of tube voltage in X-ray dark-field chest radiography," *Sci. Rep.*, vol. 9, no. 1, p. 8699, 2019.

[37] P. Meyer, T. Beckenbach, F. An, T. Schröter, J. Schulz, and J. Mohr, "X-ray gratings for grating-based X-ray DPCI fabricated using the deep X-ray lithography process: State of the art," in *Proc. XNPIG*, 2017, pp. 1–2.

[38] F. J. Koch *et al.*, "Note: Gratings on low absorbing substrates for X-ray phase contrast imaging," *Rev. Sci. Instrum.*, vol. 86, Dec. 2015, Art. no. 126114.

[39] Z. Shi, K. Jefimovs, L. Romano, and M. Stampanoni, "Towards the fabrication of high-aspect-ratio silicon gratings by deep reactive ion etching," *Micromachines*, vol. 11, no. 9, p. 864, 2020.

[40] Z. Shi, K. Jefimovs, L. Romano, J. Vila-Comamala, and M. Stampanoni, "Laboratory X-ray interferometry imaging with a fan-shaped source grating," *Opt. Lett.*, vol. 46, pp. 3693–3696, Aug. 2021.

[41] A. Malecki, G. Potdevin, and F. Pfeiffer, "Quantitative wave-optical numerical analysis of the dark-field signal in grating-based X-ray interferometry," *Europhy. Lett.*, vol. 99, p. 48001, Aug. 2012.

[42] A. Ritter *et al.*, "Simulation framework for coherent and incoherent X-ray imaging and its application in Talbot-Lau dark-field imaging," *Opt. Exp.*, vol. 22, pp. 23276–23289, Sep. 2014.

[43] J. Rieger *et al.*, "Designing the phase grating for Talbot-Lau phase-contrast imaging systems: A simulation and experiment study," *Opt. Exp.*, vol. 24, p. 13357, Jun. 2016.

[44] Z. Wu *et al.*, "Prototype system of noninterferometric phase-contrast computed tomography utilizing medical imaging components," *J. Appl. Phys.*, vol. 129, Feb. 2021, Art. no. 074901.

[45] D. Paganin, *Coherent X-Ray Optics*. Oxford, U.K.: Oxford Univ. Press.

[46] M. Engelhardt *et al.*, "High-resolution differential phase contrast imaging using a magnifying projection geometry with a micro-focus X-ray source," *Appl. Phys. Lett.*, vol. 90, May 2007, Art. no. 224101.

[47] J. Dittmann, A. Balles, and S. Zabler, "Optimization based evaluation of grating interferometric phase stepping series and analysis of mechanical setup instabilities," *J. Imag.*, vol. 4, p. 77, Jun. 2018.

[48] T. Weber *et al.*, "Noise in X-ray grating-based phase-contrast imaging," *Med. Phys.*, vol. 38, no. 7, pp. 4133–4140, 2011.

[49] S. Pinzek *et al.*, "Fabrication of X-ray absorption gratings via deep X-ray lithography using a conventional X-ray tube," *J. Micro/Nanopatterning, Mater., Metrol.*, vol. 20, Oct. 2021, Art. no. 043801.

[50] V. Revol *et al.*, "X-ray interferometer with bent gratings: Towards larger fields of view," *Nucl. Instrum. Methods Phys. Res. Sect. A, Accel., Spectrometers, Detectors Associated Equipment*, vol. 648, pp. S302–S305, Aug.2011.

[51] T. Weitkamp *et al.*, "X-ray phase imaging with a grating interferometer," *Opt. Exp.*, vol. 13, pp. 6296–6304, Aug. 2005.

[52] I. Zanette *et al.*, "Quantitative phase and absorption tomography with an X-ray grating interferometer and synchrotron radiation," *Phys. Status Solidi A, Appl. Mater. Sci.*, vol. 208, no. 11, pp. 2526–2532, Nov. 2011.

[53] F. Horn *et al.*, "Analysis of a deconvolution-based information retrieval algorithm in X-ray grating-based phase-contrast imaging," *Proc. SPIE*, vol. 9033, Mar. 2014, Art. no. 903351.

[54] M. von Teuffenbach *et al.*, "Grating-based phase-contrast and dark-field computed tomography: A single-shot method," *Sci. Rep.*, vol. 7, p. 7476, Aug. 2017.

[55] J. Xu, Z. Wang, S. van Gogh, M. Rawlik, S. Spindler, and M. Stampanoni, "Intensity-based iterative reconstruction for helical grating interferometry breast CT with static grating configuration," *Opt. Exp.*, vol. 30, pp. 13847–13863, Apr. 2022.

[56] C. Kottler, F. Pfeiffer, O. Bunk, C. Grünzweig, and C. David, "Grating interferometer based scanning setup for hard X-ray phase contrast imaging," *Rev. Sci. Instrum.*, vol. 78, no. 4, Apr. 2007, Art. no. 043710.

[57] *Medical Electrical Equipment—Characteristics of Focal Spots*, document DIN EN 60336, 2019.

[58] R. Behling, *Modern Diagnostic X-Ray Sources: Technology, Manufacturing, Reliability*. Boca Raton, FL, USA: CRC Press, 2021.

[59] T. Schoonjans *et al.*, "The xraylib library for X-ray–matter interactions. Recent developments," *Spectrochimica Acta B, At. Spectrosc.*, vol. 66, nos. 11–12, pp. 776–784, Nov. 2011.